

# The mechanical robustness of atomic-layer- and molecular-layer-deposited coatings on polymer substrates

David C. Miller,<sup>1,2,a)</sup> Ross R. Foster,<sup>1,2</sup> Yadong Zhang,<sup>1,2</sup> Shih-Hui Jen,<sup>2,3</sup> Jacob A. Bertrand,<sup>2,3</sup> Zhixing Lu,<sup>1,2</sup> Dragos Seghete,<sup>2,3</sup> Jennifer L. O'Patchen,<sup>2,3</sup> Ronggui Yang,<sup>1,2</sup> Yung-Cheng Lee,<sup>1,2</sup> Steven M. George,<sup>2,3</sup> and Martin L. Dunn<sup>1,2</sup>

<sup>1</sup>Department of Mechanical Engineering, University of Colorado, Boulder, Colorado 80309, USA

<sup>2</sup>DARPA Center for Integrated Micro/Nano-Electromechanical Transducers (iMINT), University of Colorado, Boulder, Colorado 80309, USA

<sup>3</sup>Department of Chemistry and Biochemistry, University of Colorado, Boulder, Colorado 80309, USA

(Received 26 January 2009; accepted 26 March 2009; published online 12 May 2009)

The mechanical robustness of atomic layer deposited alumina and recently developed molecular layer deposited aluminum alkoxide (“alucone”) films, as well as laminated composite films composed of both materials, was characterized using mechanical tensile tests along with a recently developed fluorescent tag to visualize channel cracks in the transparent films. All coatings were deposited on polyethylene naphthalate substrates and demonstrated a similar evolution of damage morphology according to applied strain, including channel crack initiation, crack propagation at the critical strain, crack densification up to saturation, and transverse crack formation associated with buckling and delamination. From measurements of crack density versus applied tensile strain coupled with a fracture mechanics model, the mode I fracture toughness of alumina and alucone films was determined to be  $K_{IC}=1.89\pm0.10$  and  $0.17\pm0.02$  MPa m<sup>0.5</sup>, respectively. From measurements of the saturated crack density, the critical interfacial shear stress was estimated to be  $\tau_c=39.5\pm8.3$  and  $66.6\pm6.1$  MPa, respectively. The toughness of nanometer-scale alumina was comparable to that of alumina thin films grown using other techniques, whereas alucone was quite brittle. The use of alucone as a spacer layer between alumina films was not found to increase the critical strain at fracture for the composite films. This performance is attributed to the low toughness of alucone. The experimental results were supported by companion simulations using fracture mechanics formalism for multilayer films. To aid future development, the modeling method was used to study the increase in the toughness and elastic modulus of the spacer layer required to render improved critical strain at fracture. These results may be applied to a broad variety of multilayer material systems composed of ceramic and spacer layers to yield robust coatings for use in chemical barrier and other applications. © 2009 American Institute of Physics. [DOI: 10.1063/1.3124642]

## I. INTRODUCTION

Nanometer-scale thick films grown using the atomic layer deposition (ALD) technique<sup>1–4</sup> have found application as high  $\kappa$  dielectrics within the field of integrated circuit technology.<sup>5</sup> The recently developed technique known as molecular layer deposition (MLD)<sup>6,7</sup> may be used to create organic-based, polymerlike films. ALD and/or MLD coatings have been proposed for a broad range of applications, including the surface modification of compliant substrates,<sup>8,9</sup> nanoparticles or nanotubes,<sup>10,11</sup> porous films/membranes,<sup>11,12</sup> and microsystems.<sup>13</sup> Such coatings may be used to tailor characteristics including chemical permeation, charge dissipation, surface adhesion, chemical absorption, or tribological (wear-resistance). Of these, a chemical barrier coating could consist of a single layer, such as ALD alumina. Alternately, MLD aluminum alkoxide (“alucone”)<sup>6</sup> may be interposed between ceramic layers,<sup>8,9</sup> mechanically decoupling the layers thereby increasing the critical strain associated with film cracking,<sup>14</sup> while also creating a more tortuous path that limits the permeation of chemical species.<sup>15</sup>

The mechanical properties of alumina<sup>16,17</sup> and alucone<sup>18</sup> films (including modulus and coefficient of thermal expansion) have been examined recently, whereas the permeability of alumina films has been examined separately.<sup>8,9</sup> From these studies, ALD and/or MLD permeation barriers are expected to benefit from the characteristics unique to the deposition techniques, i.e., the resulting films are continuous, conformal, pin-hole free, and may be grown with subnanometer thickness control. In particular, alumina should be less permeable based on its amorphous microstructure,<sup>4</sup> i.e., it lacks grain boundaries. Alternately, the covalent bonding present between alumina and alucone<sup>6</sup> is expected to result in improved interfacial adhesion, essential to a permeation barrier. The mechanical robustness of alumina and alucone coatings specific to the chemical barrier application has not been previously examined.

Failure modes for a film on a substrate include delamination, channel cracking, spalling of the film/substrate system, simultaneous wrinkling of the film and substrate, and buckling combined with delamination.<sup>19–23</sup> Additional microstructure-specific mechanisms that may relieve stress within a film, such as dislocation propagation and stacking fault activity,<sup>24</sup> are not applicable to alumina coatings, be-

<sup>a)</sup>Electronic mail: dcm@colorado.edu.

Report Documentation Page				Form Approved OMB No. 0704-0188	
Public reporting burden for the collection of information is estimated to average 1 hour per response, including the time for reviewing instructions, searching existing data sources, gathering and maintaining the data needed, and completing and reviewing the collection of information. Send comments regarding this burden estimate or any other aspect of this collection of information, including suggestions for reducing this burden, to Washington Headquarters Services, Directorate for Information Operations and Reports, 1215 Jefferson Davis Highway, Suite 1204, Arlington VA 22202-4302. Respondents should be aware that notwithstanding any other provision of law, no person shall be subject to a penalty for failing to comply with a collection of information if it does not display a currently valid OMB control number.					
1. REPORT DATE <b>MAR 2009</b>		2. REPORT TYPE		3. DATES COVERED <b>00-00-2009 to 00-00-2009</b>	
4. TITLE AND SUBTITLE <b>The mechanical robustness of atomic-layer- and molecular-layer-deposited coatings on polymer substrates</b>				5a. CONTRACT NUMBER	
				5b. GRANT NUMBER	
				5c. PROGRAM ELEMENT NUMBER	
6. AUTHOR(S)				5d. PROJECT NUMBER	
				5e. TASK NUMBER	
				5f. WORK UNIT NUMBER	
7. PERFORMING ORGANIZATION NAME(S) AND ADDRESS(ES) <b>University of Colorado, Department of Chemistry and Biochemistry, Boulder, CO, 80309</b>				8. PERFORMING ORGANIZATION REPORT NUMBER	
9. SPONSORING/MONITORING AGENCY NAME(S) AND ADDRESS(ES)				10. SPONSOR/MONITOR'S ACRONYM(S)	
				11. SPONSOR/MONITOR'S REPORT NUMBER(S)	
12. DISTRIBUTION/AVAILABILITY STATEMENT <b>Approved for public release; distribution unlimited</b>					
13. SUPPLEMENTARY NOTES					
14. ABSTRACT					
15. SUBJECT TERMS					
16. SECURITY CLASSIFICATION OF:			17. LIMITATION OF ABSTRACT <b>Same as Report (SAR)</b>	18. NUMBER OF PAGES <b>12</b>	19a. NAME OF RESPONSIBLE PERSON
a. REPORT <b>unclassified</b>	b. ABSTRACT <b>unclassified</b>	c. THIS PAGE <b>unclassified</b>			

cause of their amorphous nature. The aforementioned failure modes are known to depend upon the elastic mismatch between the film and substrate, i.e., the Dunder's parameters, Eqs. (1) and (2).<sup>20</sup>

$$D_1 = \frac{\overline{E_f} - \overline{E_s}}{\overline{E_f} + \overline{E_s}}. \quad (1)$$

$$D_2 = \frac{1}{2} \frac{E_f(1 + \nu_s)(1 - 2\nu_s) - E_s(1 + \nu_f)(1 - 2\nu_f)}{E_f(1 + \nu_s)(1 - \nu_s) + E_s(1 + \nu_f)(1 - \nu_f)}. \quad (2)$$

The effective modulus of the film or substrate may be understood according to the condition of plane strain typically present, Eq. (3).

$$\overline{E_i} = \frac{E_i}{(1 - \nu_i^2)}. \quad (3)$$

The energy release rate associated with the applied- and residual-mechanical conditions is represented in Eq. (4).<sup>19</sup>

$$G = \frac{\pi h_f}{2E_f} \left( \frac{E_f \varepsilon_o}{1 - \nu_f^2} + \sigma_r \right)^2 g[D_1, D_2]. \quad (4)$$

In comparison, the energy release rate required to fracture the strained film is given in Eq. (5).

$$\Gamma = \frac{K_{IC}^2}{E_f}. \quad (5)$$

In the equations, here for the international system of units,  $D$  represents the Dunder's parameters (unitless),  $E$  is the elastic modulus (Pa),  $\nu$  is the Poisson's ratio (unitless),  $G$  is the energy release rate (Pa m),  $\pi$  is the mathematical constant,  $h$  is the thickness (m),  $\varepsilon_o$  is the applied strain (m/m),  $\sigma_r$  is the residual stress within the film (Pa), the coefficient  $g$  accounts for elastic misfit between the film and substrate (unitless),<sup>19</sup>  $\Gamma$  is the critical energy release rate (Pa m), and  $K_{IC}$  the mode I fracture toughness of the film (Pa m<sup>0.5</sup>). The subscripts  $f$ ,  $s$ , and  $i$  refer to the film, substrate, or arbitrary layers, respectively. When residual stress is absent, the applied strain  $\varepsilon_o$  in Eq. (4) equals the critical strain  $\varepsilon_c$ .

The minimally sufficient condition required for catastrophic failure is realized when Eqs. (4) and (5) first become equal, where an isolated channel crack will propagate spontaneously across the width of the film, in the direction perpendicular to the applied strain. With increasing tensile strain, a series of parallel channel cracks will form. For low crack densities, the elastic fields surrounding the cracks will not interact and the process of crack densification may be analyzed according to a Weibull statistical representation.<sup>25,26</sup> Cracks may be considered isolated if their spacing,  $\lambda$  exceeds  $(3\pi h_f/2)g[D_1, D_2]$ , i.e.,  $\lambda > 8$  to  $25h_f$ .<sup>21,27-29</sup> At high crack densities, the elastic fields surrounding the cracks may interact and the crack spacing may be related to the applied deformation according to concerted or sequential crack formation representations.<sup>21,22,27-30</sup> For extensive strain, the minimum spacing between cracks becomes limited by the transfer of load along its interface with the substrate such that the stress within the interior of the film equals the stress present according to the applied loading conditions, i.e.,  $\sigma = E_f \varepsilon_o + \sigma_r$ . At the condition of crack

saturation, where the crack density is no longer increased with strain, a shear-lag model may be used to relate between the maximum shear across the load transfer region and the applied load,<sup>31-34</sup> Eq. (6).

$$\frac{c_1[D_1]\sigma h_f}{\lambda_{\min}} \leq \tau_c \leq \frac{2c_1[D_1]\sigma h_f}{\lambda_{\min}}. \quad (6)$$

New parameters in the equation include the coefficient  $c_1$  (unitless),  $\sigma$  as the net stress present in the far field (Pa),  $\tau_c$  as the critical interfacial shear between the film and substrate (Pa), and  $\lambda_{\min}$  as the minimum crack spacing (m). Applying to the case of a stiff film on a compliant substrate,  $c_1$  may be obtained from Fig. 9 in Beuth and Klingbeil<sup>34</sup> to account for more complex slip/crack interaction associated with plastic deformation of the substrate, which is not considered in the linear stress/slip length profile used in the standard shear-lag representation.<sup>32,34</sup>

In addition to channel cracking, the Poisson's effect dictates that the film will be affected in the direction orthogonal to the applied deformation.<sup>26,35</sup> In the case of poor interfacial adhesion, the film may immediately delaminate in conjunction with buckling and/or cracking.<sup>20,36</sup> In the case of a compliant substrate, the film and substrate may instead remain adhered after mechanically buckling.<sup>23,37,38</sup> In this "wrinkled" configuration, the film may fracture at the periodic wave peaks. Therefore, whether or not the film remains adhered to the substrate, a series of transverse cracks may come to exist in the direction parallel to the applied deformation. For an elastic film and substrate, the strain required to initiate buckling  $\varepsilon_b$  may be estimated from Eq. (7).<sup>23,37,38</sup>

$$\varepsilon_b = \frac{1}{4} \left( \frac{3\overline{E_s}}{\overline{E_f}} \right)^{2/3} \quad (7)$$

In the case of a film on a very compliant substrate, i.e.,  $D_1 \rightarrow 1$ , certain characteristics of mechanical failure may become accentuated. For channel cracks as well as delamination,  $g$  [Eq. (4)] may be increased by more than an order of magnitude, thereby increasing the energy release rate and decreasing  $\varepsilon_c$ .<sup>39,40</sup> Also, the crack length required to reach the condition of steady state propagation, ordinarily  $\sim 4h_f$ ,<sup>29,41</sup> is greatly increased for a stiff film on a compliant substrate. Hence, the length of interior-located cracks may be increased by an order of magnitude before escaping arrest, whereas edge-located cracks may lengthen by two orders of magnitude before achieving steady state propagation. Furthermore, the region of influence surrounding an isolated crack will be increased as will the distance associated with interfacial shear, Eq. (6). Unlike for  $D_1 < 0$ , the condition of a stiff film additionally increases the likelihood that cracks will extend through the thickness of the film up to the interface with the substrate.<sup>19</sup> In addition to the aforementioned solutions, e.g.,<sup>19-22</sup> a unique solution specific to the case of very high  $D_1$  values has been recently developed.<sup>30</sup> The characteristics associated with  $D_1 \rightarrow 1$ , including reduced  $\varepsilon_c$ , increased length prior to spontaneous crack propagation and increased interaction zone between cracks will be further compounded by inelastic behavior within the substrate, which makes the characteristics more pronounced.<sup>30,34,39,40</sup>

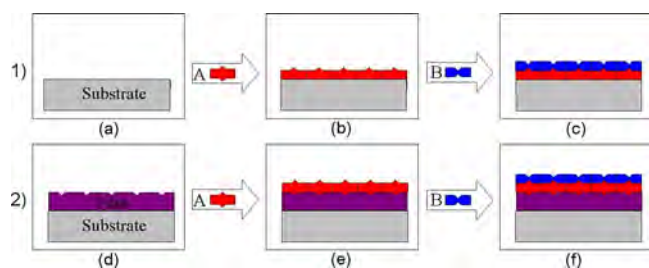


FIG. 1. (Color online) Schematic showing the subreaction sequence resulting in the growth of ALD or MLD coatings. Films are grown in monolayer increments by alternating between two separate half reactions, i.e., “A” and “B” surface species.

The goal of this study is to examine the mechanical robustness of alumina and alucone coatings subject to prescribed uniaxial mechanical elongation. First, monolayer coatings will be used to determine the behavior of each material. Second, the two materials will be incorporated into a multilayer architecture, with the goal of increasing the maximum critical strain prior to failure. Third, the performance of the multilayer composite will be compared to a recent model based on a multilayer thin-film fracture mechanics analysis. The model will be used to identify the characteristics of the ideal spacer layer material. While the study here examines a three-layer architecture consisting of specific materials, the basic behavior is expected to apply broadly to more complicated architectures composed of other materials.

## II. EXPERIMENTAL

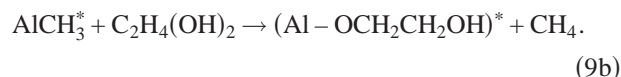
Films were deposited in a viscous flow reactor using the ALD<sup>1–4</sup> or MLD<sup>6</sup> techniques. The coating techniques do not require line of sight for deposition and are deposited in blanket format. The deposition techniques are based on a sequence of two self-limiting reactions between vapor-phase precursor molecules and a solid surface, as shown schematically in Fig. 1. For alumina, film growth proceeds according to the two half reactions, Eqs. (8a) and (8b), where the asterisks designate the surface species.<sup>3,4</sup>



The reactants, trimethyl aluminum [TMA,  $\text{Al}(\text{CH}_3)_3$ ] and water ( $\text{H}_2\text{O}$ ), are alternately injected via nitrogen carrier gas. Using computer-controlled pneumatic valves, the substrate surface is first exposed to reactant A, Fig. 1(b), which reacts with the active surface sites. Then, after purging the by products from reaction A, the surface is exposed to reactant B, Fig. 1(c). This reaction regenerates the initial functional groups, preparing the surface for the next exposure to reactant A, Fig. 1(e). The film is grown to the desired thickness by repeating the AB sequence. For alucone, film growth proceeds similarly according to the two half reactions, Eqs. (9a) and (9b), where the initial reactant species are TMA and ethylene glycol [ $\text{EG}$ ,  $\text{C}_2\text{H}_4(\text{OH})_2$ ].<sup>6,7</sup>



FIG. 2. (Color online) A chemical tag was used for the postexamination of tensile specimens. A lipophilic end group enables the tag to adhere specifically to the hydrophobic surface of the PEN substrate; a fluorescent end group enables damage visualization via external illumination.



For the 4.7 l chamber, the dose time of 1, 0.2, or 120 s were utilized for TMA,  $\text{H}_2\text{O}$ , or EG, respectively, at the injection pressure of 300 mTorr. Dosing was followed by purging with ultrahigh purity  $\text{N}_2$  at the injection pressure of 300 mTorr for 75 s. The growth temperature of 155 °C and baseline chamber pressure of 650 mTorr were utilized for all experiments. Direct deposition, with no substrate surface treatment, was performed after stabilizing the temperature overnight.

Alumina, alucone, or alumina/alucone/alumina coatings were grown on 75  $\mu\text{m}$  thick polyethylene naphthalate (PEN) (Dupont Teijin Inc.) substrates. In particular, the optical grade “Teonex Q65” is commonly used in the organic light emitting diode (OLED) field because it is both heat stabilized and coated with a scratch resistant layer on its top surface.<sup>42,43</sup> Similar to the standard method for tensile testing of thin plastic materials,<sup>44</sup> coated PEN sheets were cut into strips (50 × 10 mm<sup>2</sup> gage section) using a paper cutter. Other methods such as die stamping or laser cutting to the American Society for Testing and Materials (ASTM) D638–03 (type IV) profile<sup>45</sup> proved unsuccessful because of the toughness of or damage to the PEN substrate. As in the method 45, each specimen strip was then tensioned in ambient (25 °C) to a prescribed strain  $\epsilon_o$  at the displacement controlled strain rate of 0.015 s<sup>–1</sup> using a mechanical load-frame (Insight 2, MTS Systems Corp.) while being measured using a laser extensometer (LE-05, Electronic Instrument Research Corp.). To prevent fracture related to the sharp grip teeth, polymer strips (“Flex-o-Pane,” Warp Brothers, Inc.) were attached over the grip ends outside of the gage region of the specimens using epoxy (E6000, Eclectic Products, Inc.).

As the thickness of the film coatings renders them optically transparent, damage was inspected using a recently developed fluorescent tag.<sup>46</sup> The tag has a specifically designed lipophilic moiety that facilitates selective binding to damage sites based on the surface adhesion characteristics of the material system. As illustrated in Fig. 2, the tag binds to the PEN substrate, not alumina or alucone, based on its greater hydrophobicity. The tag molecules also bear a fluorescent moiety, with primary emission at the optical wavelength of 515 nm. In addition, the tag has a small molecule size, i.e., molecular weight of ~300, allowing molecules to enter easily into nanometer-scale damage sites. To verify its validity,



the fluorescent tag method was compared with the optical visualization method described by others,<sup>47–49</sup> which incorporates an oxygen plasma etch to undercut the substrate at damage sites. In that method, oxygen ions pass through damaged regions of the film and consume the substrate, rendering the damage visible in an optical microscope. After comparing instances of the same damaged region, the tag was chosen over the plasma etching method based on its ability to obviate finer features as well as the greater contrast rendered by the tag.<sup>46</sup>

The procedure for damage inspection is as follows. The top surface of coated specimens, previously tensioned to  $\varepsilon_o$ , was soaked in a 2.9% volume (tag:ethanol) solution for 5 min. A 70:30 vol % (ethanol:de-ionized water) solvent solution was then used to wash away the excess tag. The sample was then dried using clean dry air and maintained in an ultraviolet-safe environment. Fluorescent emission was measured using a confocal microscope (LSM 510, Carl Zeiss, Inc.) equipped with an argon/2 laser ( $\lambda=488$  nm). The average crack spacing was determined from the number of cracks within a known sample size region, where the final value  $\lambda_{\text{avg}}$  was the average of six measurements (top, middle, and bottom of two separate images).

### III. MODELING

In addition to the aforementioned analytical models, the failure of thin film(s) may be understood according to a recently developed fracture mechanics based formalism.<sup>14</sup> As in the analytic representation, Eq. (4), and other equivalent models,<sup>20–22</sup> the  $\varepsilon_o$  required to propagate a crack may be determined from the associated change in energy. In the method here, the energy associated with fracture may be determined from combination of the stress present in the region ahead of the crack tip and the displacement present in the wake remaining far behind a propagated crack, Eq. (10).

$$U = \frac{1}{2} \int \sigma[y] \delta[y] \partial y. \quad (10)$$

The total energy will scale according to the number of layers present, Eq. (11), which may be related to the applied- and residual-mechanical conditions, Eq. (12).

$$U = n_i h_i \Gamma_c + n_j h_j \Gamma_p, \quad (11)$$

$$U = (\bar{E}_f \varepsilon_o + \sigma_r) \left( \varepsilon_o + \frac{\sigma_r}{E_f} \right) h_f^2 f \left[ \frac{h_p}{h_f}, \frac{E_p}{E_f} \right]. \quad (12)$$

New parameters introduced in the equations include  $U$  as the energy (J),  $\delta$  as the displacement in profile along the crack face (m),  $y$  as the through-thickness axis location (m),  $n$  as the number of material layers (unitless), and  $f$  as a dimensionless function specific to the geometry and materials. Additional notation includes the indices  $i$  and  $j$  as well as the subscripts  $c$  and  $p$ , which represent the ceramic and polymerlike spacer layers, respectively. The numerical analysis (ABAQUS, Dassault Systèmes Inc.) was conducted using an automated routine (PYTHON, Python Software Foundation). Analysis here was solely limited to the linear elastic regime for all materials considered.

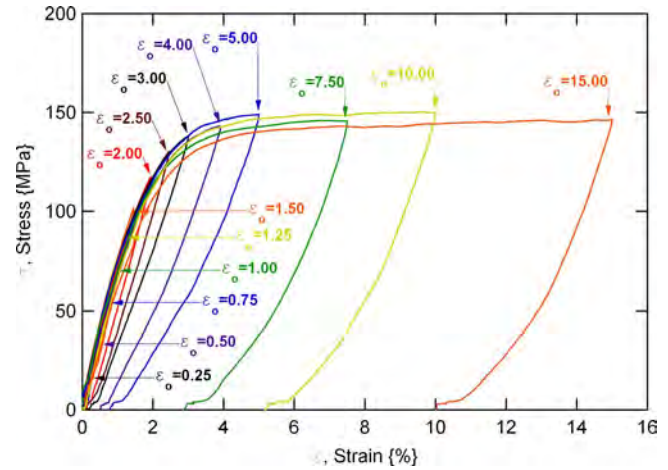


FIG. 3. (Color online) Tensile test data (engineering stress/strain) for a 5 nm thick  $\text{Al}_2\text{O}_3$  layer deposited on a 75  $\mu\text{m}$  thick PEN substrate.

## IV. RESULTS AND DISCUSSION

### A. Alumina monolayer deposited on PEN

Figure 3 shows the tensile results for a set of separate strips of alumina deposited on PEN, identifying the stress/strain relationship as the specimens were tensioned to  $\varepsilon_o$  and then more rapidly unloaded to 0% strain. Figure 3 identifies the initial  $\varepsilon_o$  values used to evaluate all coatings, whereupon subsequent iterative tests were always used to identify the onset of damage to within 1/8% strain. Because  $h_s$  is at least three orders of magnitude greater than  $h_f$ , the mechanical response in Fig. 3 applies to the PEN substrate. Therefore, from the standard test protocol,<sup>45</sup> the elastic modulus of PEN is  $8.4 \pm 1.5$  GPa and the flow stress at the applied strain of 8% is  $141 \pm 8$  MPa. Instrumented indentation was performed according to the procedure in Ref. 17 to further examine the properties of the substrate material. Using a numerical postprocessing algorithm,<sup>50</sup> the hardness of  $0.45 \pm 0.03$  GPa, yield strength of  $207 \pm 0.03$  MPa, and yield strain of 4.6% were identified for PEN. Because of the viscoelastic nature of polymeric materials, the characteristics of PEN depend upon the loading rate and temperature used during testing.

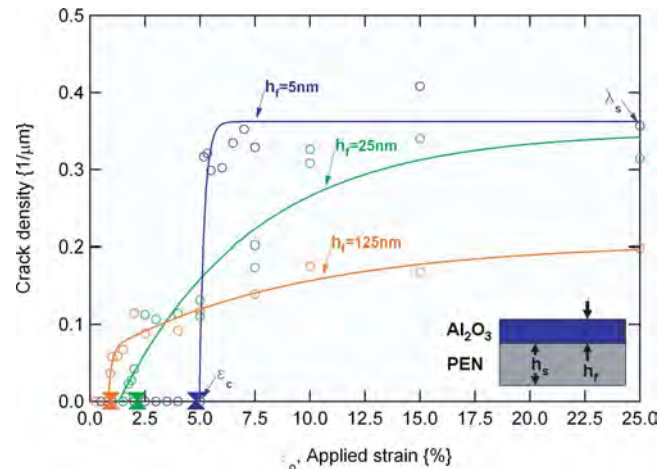


FIG. 4. (Color online) Measured crack density for a single  $\text{Al}_2\text{O}_3$  layer (deposited on a 75  $\mu\text{m}$  thick PEN substrate), following tensile testing to prescribed strains.

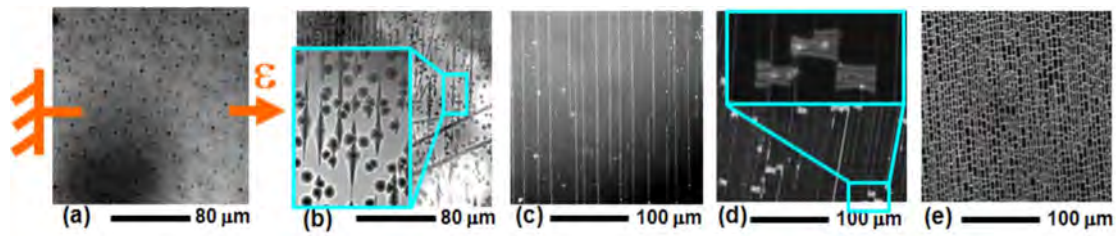


FIG. 5. (Color online) Evolution of the damage morphology for a single 125 nm thick  $\text{Al}_2\text{O}_3$  layer deposited on PEN. The set of images includes separate specimens tensioned to the  $\varepsilon_o$  of (a) 0%, (b) 0.9%, (c) 1.5%, (d) 7.5%, and (e) 25%.

The modulus values of 195.3 and 36.8 GPa for alumina<sup>17</sup> and alucone,<sup>18</sup> determined separately using indentation, combined with that of the substrate dictates the  $D_1$  values [Eq. (1)] of 0.91 and 0.62, respectively. The resulting configuration for a monolayer ALD or MLD coating on PEN is therefore that of a stiff material on a very compliant substrate. Second, the macroscopic response for the strips is dominated by the inelastic behavior of PEN. In particular, the inelastic behavior is dominant above the  $\varepsilon_o$  of 4.6%, where the final strain becomes greatly increased with applied strain for  $\varepsilon_o > 4\%$ .

Tensioned specimens were then examined using the fluorescent tag and the channel crack density ( $1/\lambda_{\text{avg}}$ ) was measured according to  $\varepsilon_o$ , as shown in Fig. 4. Three different coating thicknesses ( $h_f=5$ , 25, and 125 nm) were studied. Specifically labeled in the figure for 5 nm alumina, cracks begin to readily propagate at  $\varepsilon_c$ , and their density saturates at  $\lambda_s$ . The results of a trendline fit are provided in Fig. 4 to guide the eye, but do not imply a specific relationship. Lastly, the results of numerical analysis, using the average of the measured  $K_{\text{IC}}$  values for alumina (below), are indicated in the figure with a hourglass. Specifically, the  $\varepsilon_c$  of 0.97%, 2.17%, and 4.85% are identified for 5, 25, and 125 nm thick  $\text{Al}_2\text{O}_3$ , respectively.

Using the 125 nm thick alumina coating as an example, the evolution of the damage morphology is shown in Fig. 5. The set of images includes separate specimens tensioned to the  $\varepsilon_o$  of 0% in Fig. 5(a), where the surface roughness of the PEN as well as contamination are rendered apparent, 0.9% in Fig. 5(b), where the first channel cracks have already propagated and others are initiating, 1.5% in Fig. 5(c), showing continued crack densification, 7.5% in Fig. 5(d), where transverse cracks have formed, and 25% in Fig. 5(e), where a dense network of both channel and transverse cracks is evident. The details of crack propagation about defects at the surface or transverse crack formation are shown separately in the insets of Fig. 5(b) or Fig. 5(d), respectively. Image (b) identifies crack nucleation (but not propagation) and is specific to defects, contamination, or antiblock particles at the

surface, whereas image (d) identifies the localized three-dimensional (buckled) geometry motivating transverse crack formation. Images (a) and (b) were rendered using an oxygen plasma etching method,<sup>47–49</sup> while images (c)–(e) were rendered using the chemical tag method, Fig. 2.

The results for alumina are further summarized in Table I, which identifies  $\varepsilon_c$ , the critical strain for steady state channel crack propagation,  $R_c$ , the equivalent critical bending radius for  $h_s=75 \mu\text{m}$ ,  $\delta_c$ , the predicted crack opening displacement at  $\varepsilon_c$ ,  $\Gamma$ , the critical energy release rate,  $K_{\text{IC}}$ , the mode I fracture toughness for alumina,  $\varepsilon_t$ , the critical strain for transverse cracking,  $\lambda_s$ , the saturated crack spacing, and,  $\tau_c$ , the critical interfacial shear between alumina and PEN.  $R_c$ , an engineering quantity often specified for design and safe application, was determined from Eq. (13).

$$R_c = \frac{(hf + h_s)}{2\varepsilon_c}. \quad (13)$$

The predicted crack opening displacement was estimated analytically according to the previously developed method.<sup>19</sup>  $\Gamma$  was determined at  $\varepsilon_c$ , i.e., when Eq. (4) becomes equal to Eq. (5).  $K_{\text{IC}}$  follows from  $\Gamma$  according to Eq. (5).  $\varepsilon_t$  was determined to within a few percent strain relative to the onset of cracking, e.g., Fig. 5(e). If the three different coatings are considered collectively, then  $\Gamma = 18.6 \pm 1.9$ ,  $K_{\text{IC}} = 1.89 \pm 0.10$ , and  $\tau_c = 39.5 \pm 8.3$  for alumina.

For alumina,  $\varepsilon_c$  is observed to increase as  $h_f$  is decreased, as suggested in Eq. (4). Specifically, the critical strain of 5% for  $h_f=5$  nm is notably greater than the  $\varepsilon_c$  of 0.5%–2% commonly observed in the literature for conventional (micrometer scale) thin film materials<sup>51</sup> including  $\text{SiO}_2$ ,<sup>26</sup>  $\text{Si}_3\text{N}_4$ ,<sup>49</sup> indium tin oxide,<sup>51,52</sup> and amorphous Si.<sup>53</sup> The greater  $\varepsilon_c$  for the 5 nm thick alumina film is attributed to its nanometer-scale thickness, allowed by the ALD technique. In contrast,  $K_{\text{IC}}$  for bulk crystalline  $\text{Al}_2\text{O}_3$  typically ranges from 4–6  $\text{MPa m}^{0.5}$ ,<sup>54</sup> however  $K_{\text{IC}}$  of 1.7 and 1.4  $\text{MPa m}^{0.5}$  was measured for amorphous thin films created via the physical vapor deposition and thermal decompo-

TABLE I. Summary of results for a single  $\text{Al}_2\text{O}_3$  layer (deposited on PEN), tensioned to prescribed strains.

$h_f$ (nm)	$\varepsilon_c$ (%)	$R_c$ (mm)	$\delta_c$ (nm)	$\Gamma$ (J/m <sup>2</sup> )	$K_{\text{IC}}$ (MPa m <sup>0.5</sup> )	$\varepsilon_t$ (%)	$\lambda_s$ ( $\mu\text{m}$ )	$\tau_c$ (MPa)
5	$5.08 \pm 0.08$	0.64	6.8	$25.3 \pm 0.8$	$2.22 \pm 0.04$	$12.5 \pm 2.5$	$2.8 \pm 0.1$	$25.0 \pm 1.8$
25	$1.56 \pm 0.06$	2.40	10.4	$11.9 \pm 1.0$	$1.53 \pm 0.06$	$6.25 \pm 1.25$	$3.2 \pm 0.2$	$32.3 \pm 4.3$
125	$0.88 \pm 0.06$	4.30	29.2	$18.7 \pm 1.9$	$1.91 \pm 0.10$	$6.25 \pm 1.25$	$5.0 \pm 0.2$	$61.1 \pm 8.3$

sition techniques, respectively.<sup>55,56</sup>  $K_{IC}$  as reported in Table I for alumina is thought to be typical of amorphous  $Al_2O_3$ , however, toughness does not limit mechanical performance here more significantly than  $h_f$ . The difference in  $\varepsilon_c$  for 5 and 125 nm thick alumina films would be significant in applications, as this difference results in a 6.7 times decrease in the allowable radius of curvature, permitting much greater folding of the chemical barrier.  $\varepsilon_c$  is of primary importance here because a fully propagated crack would catastrophically compromise a chemical permeation barrier;<sup>57</sup> crack initiation at specific defect sites as in Fig. 5(c), which may occur for  $\varepsilon_o < \varepsilon_c$ , may also be unacceptable in certain applications.

The  $\tau_c$  for alumina/PEN is greater than the range of 1–11 MPa mentioned for thin films,<sup>27,31</sup> but is comparable with values observed for the biopolymer/ceramic system present in nacre (37–46 MPa)<sup>58</sup> or in synthetic fiber/composite systems (often 5–50 MPa).<sup>59</sup> A robust alumina/PEN interface was anticipated as the vapor phase precursors used to grow alumina were determined to permeate into the subsurface of PEN during deposition,<sup>6</sup> allowing alumina to form in the porous regions between polymer chains, greatly improving interfacial adhesion.

Regarding the data in Fig. 4, the results are similar to previous studies,<sup>26,27,31,60,57</sup> which likewise demonstrate the asymptotic densification of channel cracks up to a saturation value. For alumina, the saturation spacing is significantly greater than the film thickness, so the shape of the crack density should vary with strain according to the distribution of defects in the film,<sup>25,26</sup> rather than according to interaction between closely separated cracks.  $\varepsilon_c$ , however, depends only on the intrinsic properties of the material system and not the distribution of flaws. There is quite reasonable agreement between the measured and numerically calculated  $\varepsilon_c$  (diamonds), considering that the influence of residual stress and substrate yielding were not included in the analysis. For example, intrinsic stress as great as 474 MPa has been measured for alumina films<sup>16,17</sup> and the measured strain at yielding for PEN is  $\sim 4\%$ .

The measured  $\varepsilon_t$  is similar between the coatings of different thicknesses. Equation (7), in conjunction with the Poisson's effect, identifies  $\varepsilon_t$  to be 15.3%. As the PEN substrate yields at  $\sim 4\%$ , variation from the elastic-regime is expected, e.g.,  $\nu_s \rightarrow 0.5$ , and Eq. (7) becomes qualitative. Also,  $\varepsilon_t$  here applies to the localized condition, where defects/contamination may promote buckling, facilitate delamination, or raise stress prior to the condition of global damage.

The damage occurring when the coated PEN sheets were cut into specimen strips was explicitly examined for alumina,  $h_f = 5$  nm.  $L_e$ , the maximum length of cracks, measured from the cut edge to the interior-located tip, was

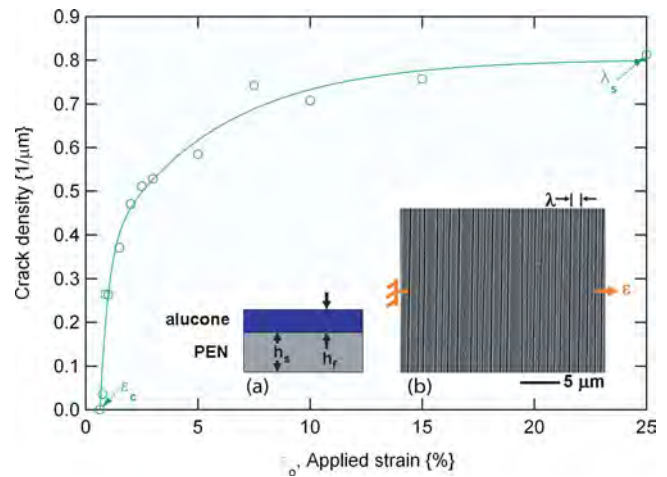


FIG. 6. (Color online) Measured crack density for a 100 nm thick alucone layer, tensioned to prescribed strains. The insets show (a) a schematic representing the specimens in cross section and (b) the morphology of the top surface (orientation is indicated with respect to  $\varepsilon_o$ ) of a specimen tensioned to  $\varepsilon_o = 25\%$ .

$159.5 \pm 35.9$   $\mu\text{m}$ , while the edge-specific crack density in the direction of the applied strain was  $0.11 \pm 0.031/\mu\text{m}$  for all  $\varepsilon_o$ . No overt trend for  $L_e$  or crack density was observed with  $\varepsilon_o$  for  $h_f = 5$  nm (or qualitatively for  $h_f = 25$  and 125 nm) and the longest edge-located cracks extended to  $\leq 4\%$  of the 10 mm sample width. The influence of sample preparation, particularly in the middle of the samples where channel crack density was determined, is therefore not significant. The lack of variation with  $\varepsilon_o$  for the edge cracks is consistent with Refs. 29 and 39, where propagation is expected to be hindered for film and substrate systems bearing a large  $D_1$  value.

## B. Alucone monolayer deposited on PEN

Like the alumina coatings, tensioned alucone specimens were examined using the fluorescent tag. The results of this examination are shown in Fig. 6, which identifies the crack density versus  $\varepsilon_o$ . Both the  $\varepsilon_c$  and  $\lambda_s$  are identified (labeled) in the figure. As in Fig. 4, a trendline fit is provided in Fig. 6 to guide the eye. Similar to Table I, key results for alucone on PEN are summarized in Table II. Unlike alumina, no transverse cracking was observed for alucone, even at  $\varepsilon_o = 25\%$ , Fig. 6(b).

For alucone, cracks were not as distinctly rendered by the fluorescent tag as they were for alumina. At greater  $\varepsilon_o$ , the crack density was verified using electron microscopy, e.g., Fig. 6(b). In contrast, initial attempts to inspect alucone deposited on polyimide (Kapton HN, DuPont, Inc.) proved unsuccessful. The tag was previously known to not adhere to polyimide.<sup>46</sup> This failed imaging scheme (tagging the film

TABLE II. Summary of results for a 100 nm thick alucone layer (deposited on PEN), tensioned to prescribed strains.

$\varepsilon_c$ (%)	$R_c$ (mm)	$\delta_c$ (nm)	$\Gamma$ (J/m <sup>2</sup> )	$K_{IC}$ (MPa m <sup>0.5</sup> )	$\lambda_s$ ( $\mu\text{m}$ )	$\tau_c$ (MPa)
$0.69 \pm 0.06$	5.46	7.7	$0.8 \pm 0.1$	$0.17 \pm 0.02$	$1.23 \pm 0.80$	$66.6 \pm 6.1$



and not the substrate), opposite of that used in Fig. 5 (tagging the substrate and not the film), indicates that the tag does not adhere to alucone.

Most interesting among the results for alucone is the brittle failure (channel cracking) observed at a modest  $\varepsilon_o = 0.69\%$ , corresponding to  $R_c = 5.46$  mm. For alucone, made according to the recently developed MLD technique,  $K_{IC}$  is estimated to be notably less than that of many polymeric materials.<sup>54</sup> From the observed damage morphology and estimated  $K_{IC}$ , alucone is expected to exhibit the stress/strain profile typical of a brittle material, i.e., sudden catastrophic failure, rather than that of a tough plastic material such as PEN (Fig. 3), i.e., significant inelastic deformation may occur prior to failure. Note that  $\Gamma$  and  $K_{IC}$  apply to the direction orthogonal to the direction of film growth. Anisotropy in properties, including  $E_f$  and  $K_{IC}$ , may exist for alucone based on its mechanism of growth. To explain, alucone is expected to form chains and/or layers that are covalently bonded in the direction of growth, whereas alucone is held together by weak hydrogen bonds in the in-plane direction.

In contrast with channel cracking, the lack of transverse cracking, indicates that (a) film/substrate buckling (“wrinkling”) does not occur, as generally suggested by Eq. (7), or (b) that the stress in such a configuration is insufficient to motivate cracking. While Eq. (7) is limited by the inelastic deformation of the PEN substrate for  $\varepsilon_o > 4\%$ , the better match in modulus between the film and substrate would be expected to increase  $\varepsilon_b$ .

The asymptotic profile in Fig. 6 suggests a load transfer limited (shear-lag) interfacial condition. Because  $\lambda_s \gg h_f$ , interaction between cracks is not expected. The crack density for alucone, which is greater than that for alumina, implies excellent interfacial adhesion between alucone and PEN, Eq. (6). As with alumina, the gaseous precursor species may permeate into the subsurface of the PEN, such that film growth originates within the porous microstructure of polymeric substrate.

### C. Assessing the tag-based inspection method from the examination of monolayer films

The data profiles, Figs. 4 and 6, as well as the damage morphology, Fig. 5, demonstrate the ability of the tag to facilitate damage inspection. For example, a crack aspect ratio ( $h_f/\delta_c$ ) ranging from 1.4 to 4.3 was readily examined for alumina, Table I. In contrast, the processing parameters for the oxygen plasma etch technique<sup>47–49</sup> must be tailored according to the aspect ratio examined, which ranged from 0.11<sup>48</sup> to 10<sup>49</sup> in the literature. In our own studies, a specimen-specific sequence of brief etches was required to utilize plasma etching for damage inspection. The tag-based examination also exceeded the ability of electron microscopy-based inspection, where inelastic strain ( $\varepsilon_o > 4\%$ ) was required open cracks beyond their initial  $\delta_c$ , enabling observation.

As in Ref. 46, however, the size (width) of the tag rendered features always exceeded the physical size of the damage, i.e., the estimated  $\delta_c$ . Further, the feature sharpness for alucone was less than that of alumina. These observations

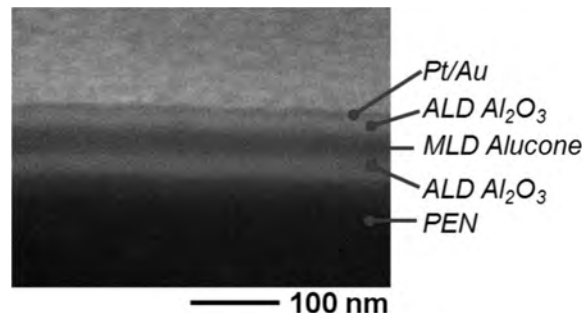


FIG. 7. Cross section of multilayer coating on PEN (micrograph is oriented obliquely to the specimen).

might be explained by the permeation of tag molecules into porous materials. For alumina, the tag became absorbed within the regions of the PEN substrate adjacent to damage sites, thereby exaggerating the feature size. Alternately, the tag may diffuse into both the alucone film and PEN substrate, rendering the materials less distinct. Disparity between observed and physical size also results in part from instrument related image diffraction.

### D. Alumina and alucone composite coatings deposited on PEN

Following the study of individual film layers, multilayer coatings were examined using the same methodology. An example of an alumina/alucone/alumina coating deposited on a PEN substrate is shown in Fig. 7, where the specimen was milled using a focused ion beam (FIB, Nova Nanolab, FEI Co.). The material layers present are labeled according to their electron contrast in the image. In Fig. 7, the measured thicknesses of 20, 29, and 24 nm for the ALD, MLD, and ALD layers agree well with the nominal thickness values of 25, 15, and 25 nm. Regarding the thickness of the MLD layer, the growth rate for alucone varies significantly with deposition temperature.<sup>6</sup>

Measured crack density versus  $\varepsilon_o$  for the alumina/alucone/alumina coatings is shown in Fig. 8, where the data profiles exhibit the same character as the single-layer coatings. The thickness of the alucone layer was varied over

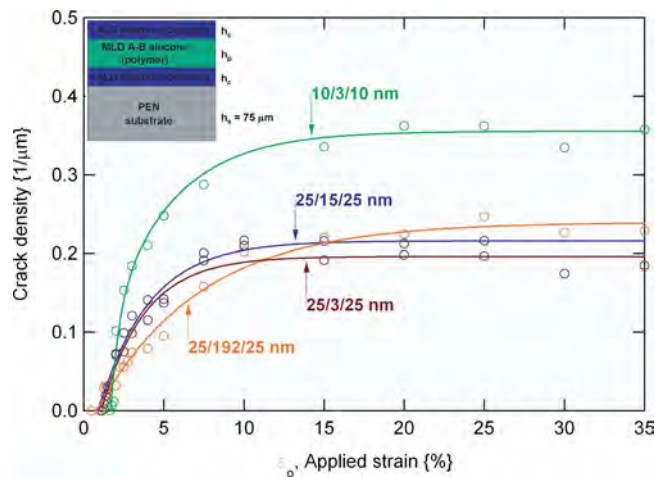


FIG. 8. (Color online) Measured crack density for separate ALD/MLD/ALD coatings (thickness  $h_c/h_p/h_c$ ), tensioned to prescribed strains.



TABLE III. Summary of results for multilayer  $\text{Al}_2\text{O}_3$ /alucone/ $\text{Al}_2\text{O}_3$  coatings, tensioned to prescribed strains.

$h_c/h_p/h_c$ (ALD/MLD/ALD)	$\varepsilon_c$ (%)	$R_c$ (mm)	$\varepsilon_t$ (%)	$\lambda_s$ ( $\mu\text{m}$ )
25/3/25	$1.19 \pm 0.06$	3.16	$4.5 \pm 0.5$	$5.08 \pm 0.12$
25/15/25	$1.31 \pm 0.06$	2.86	$6.3 \pm 1.3$	$4.63 \pm 0.24$
25/192/25	$1.19 \pm 0.06$	3.17	$6.3 \pm 1.3$	$4.38 \pm 0.18$
10/3/10	$1.69 \pm 0.06$	2.22	$6.3 \pm 1.3$	$2.76 \pm 0.25$

nearly three orders of magnitude (3–112 nm) to study its influence; the thickness of the alumina layers was also independently varied in order to ascertain its influence. Channel cracks in the composite coatings were distinctly rendered by the fluorescent tag.

Results for the composite coatings are further summarized in Table III. Transverse cracking was observed for the composite coatings, however  $\varepsilon_t$  was determined to within a few percent strain. Edge-located channel cracks generated during sample preparation were examined specifically for the 25/15/25 nm thick coating, where no significant variation was observed according to  $\varepsilon_o$ , and the values of  $250.0 \pm 48.1$  and  $14.9 \pm 6.3$   $\mu\text{m}$  were determined for  $L_e$  and  $\lambda_{s,e}$ , respectively.

The damage morphology for composite coatings is compared to that of an alumina film in Fig. 9. The representative micrograph images for specimens were obtained using an electron microscope. Similar to Fig. 9, a network of channel and transverse cracks was observed at  $\varepsilon_o=25\%$  for all of the ALD/MLD/ALD specimens examined in Fig. 8. The layers underneath the alumina surface layer were frequently observed to be torn in the region directly adjacent to transverse cracks. One such tear extends for several micrometers, Fig. 9(d). Separately, select regions of the topmost layer(s) were detached from the substrate, Fig. 9(c).

To begin discussion, the 25 nm thick alumina systems (Table III) have a lower  $\varepsilon_c$  (and corresponding greater  $R_c$ ) than the 25 nm thick alumina monolayer (Table I). The incorporation of the alucone spacer layer, which was meant to mechanically isolate two alumina layers and improve the overall strength, instead reduced  $\varepsilon_c$  for the composite system. Similarly, for a 10 nm thick alumina monolayer, Eq. (4) predicts that  $\varepsilon_c$  should exceed 3%. In contrast,  $\varepsilon_c$  for the 10 nm thick alumina composite system (Table III) was 0.6% greater than the 25 nm thick alumina composite systems (Table III). The marginal performance for the composite systems will be shown to result from the toughness of alucone.

The density characterization, Fig. 8, as well as the morphological examination, Fig. 9, identifies that channel cracks extend through the entire thickness of the composite coatings. To explain, the tag was previously found to adhere only to the PEN substrate and not the ALD or MLD coatings. Therefore, the strong fluorescent signal enabling the visualization of cracks in Fig. 8 can only be explained if the composite coatings were fractured through their entire thickness, allowing the tag to access the PEN substrate. This conclusion implies that the tears observed in Fig. 9 occur within the PEN substrate layer. Tear morphologies identical to those in

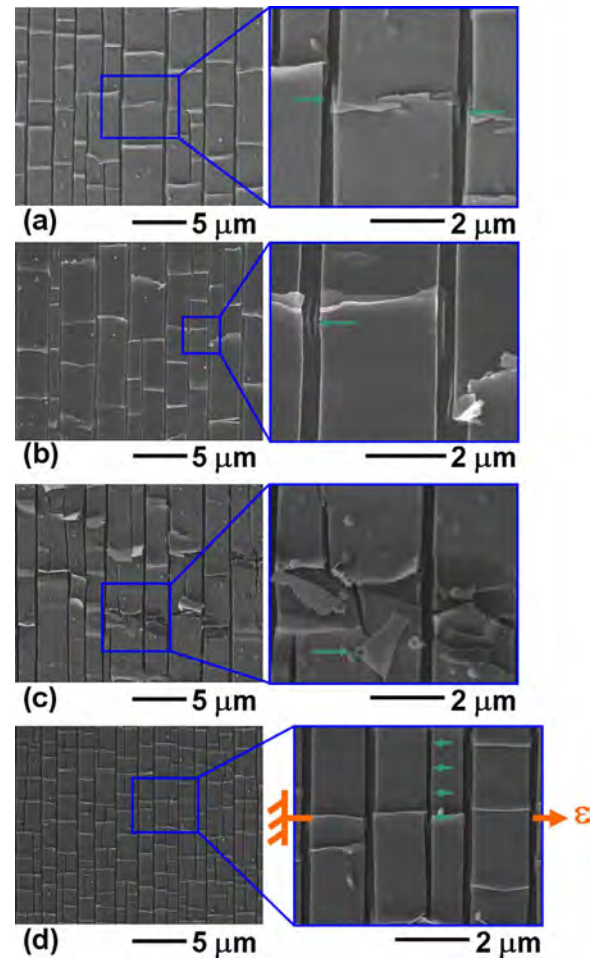


FIG. 9. (Color online) Damage morphology for coatings tensioned to  $\varepsilon_c = 25\%$ , including (a) 25 nm  $\text{Al}_2\text{O}_3$ , as well as (b) 25/15/25 nm, (c) 25/192/25, and (d) 10/3/10 nm multilayers. Tearing, concluded to occur in the PEN substrate, is indicated with an arrow in (a), (b), and (d). The delamination of film layers is shown in (c). The direction of the strain applied during testing is shown in (d).

the composite coatings, Fig. 9(b), are observed adjacent to the transverse cracks in an alumina film, Fig. 9(a), corroborating that tearing (and through-thickness fracture) is not unique to the composite coatings. In contrast, localized tearing was never observed for tensioned alucone monolayer films, therefore alucone is not expected to tear in a composite coating. Substrate tearing is consistent with the tough character of PEN (Fig. 3 and Ref. 61), which would be expected to result in localized tearing rather than brittle fracture.

Lastly, the asymptotic crack density profiles for the composite coatings, Fig. 8, indicate good adhesion between the material layers. The fractured coatings remain intact even at  $\varepsilon_o=25\%$ , well above the application limit of  $\varepsilon_c$ , but beneficial in minimizing damage associated with catastrophic impact. Although separation between the layers for the 25/192/25 nm coating is observed, Fig. 9(c), such damage is localized and not widespread. Lastly, for the 25 nm thick alumina systems, the measured  $\lambda_s$  (Table III) is similar to that observed for the 25 nm thick alumina films (Table I), suggesting that the adhesion between the bottommost alumina layer and the PEN substrate has not been compromised by the incorporation of additional MLD and ALD layers.

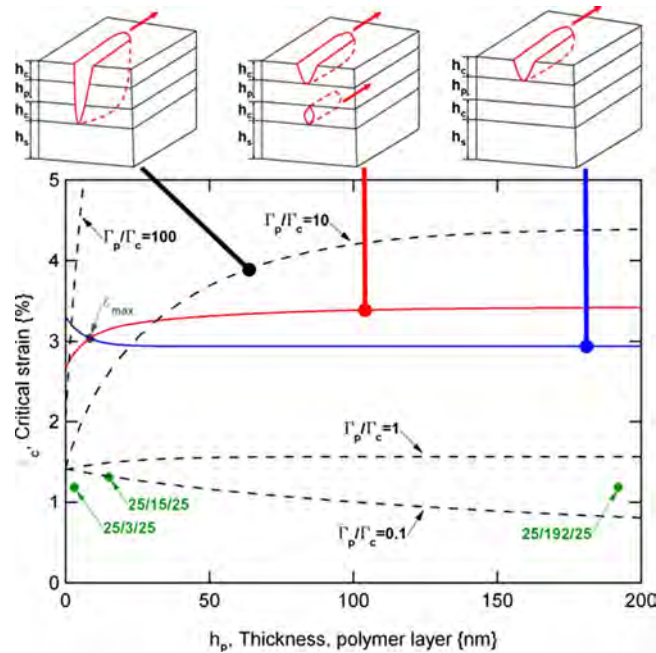


FIG. 10. (Color online) Results of numerical analysis for an ALD/MLD/ALD coating on a PEN substrate. The critical strains measured from ALD/MLD/ALD specimens, Fig. 8, are also shown in the figure.

Good adhesion between the ALD and MLD layers was expected based on the covalent bonding inherent to the deposition process, Fig. 1.

### E. Analysis of the composite coatings with consideration for future design improvements

To better understand the composite coatings, their performance was analyzed according to a recently developed fracture mechanics based formalism.<sup>14</sup> In practice, cracking may occur: (a) through the thickness of all three layers, (b) exclusively in the top ceramic layer, or (c) simultaneously in both of the ceramic layers. The input parameters, here  $E_c = 195.3$  GPa,  $\nu_c = 0.13$ ,  $\Gamma_c = 18.6$  J/m<sup>2</sup>,  $h_c = 25$  nm,  $E_p = 36.8$  GPa,  $\nu_p = 0.33$ ,  $E_s = 8.4$  GPa,  $\nu_s = 0.33$ , and  $h_s = 75$   $\mu$ m, were used to generate  $\epsilon_c$  versus  $h_p$  profiles for the three separate failure modes. The solution sets vary for the composite architecture [number of layers, Eq. (11)] according to the mode-specific geometry, Eq. (10), and also the independent parameters,  $\Gamma_p$  and  $h_p$ . The solution set bearing the lowest  $\epsilon_c$  is the failure mode expected to be realized at a particular  $h_p$ .

The results of this analysis, along with the critical strain measured from ALD/MLD/ALD specimens (Table III), are shown in Fig. 10. In the figure, which applies to linearly elastic materials, the conditions of crack formation specific to the top ceramic layer as well as simultaneous crack formation in both ceramic layers may be determined absolutely. The condition of cracking through the entire thickness of the composite coating, however, depends on the toughness of the polymer spacer layer, represented in Fig. 10 using a family of profiles.

In Fig. 10, if the thickness and toughness of the polymer spacer layer are known,  $\epsilon_c$  is predicted to occur at the minimal energy condition (either top, simultaneous, or through-

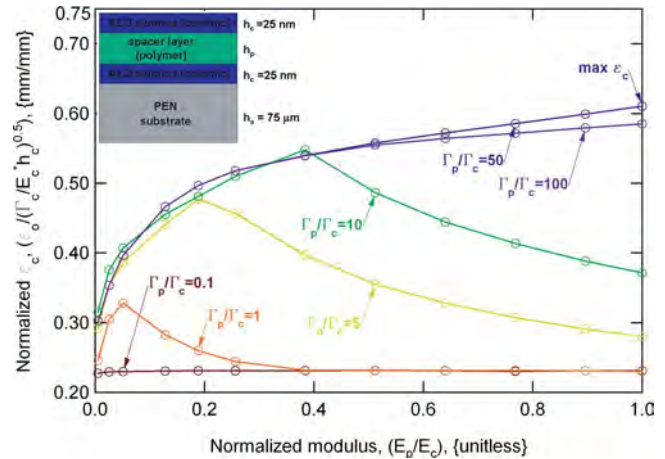


FIG. 11. (Color online) Results of numerical analysis for an alumina/arbitrary polymer/alumina coating configuration on a PEN substrate. The results predict  $\epsilon_c$  according to the modulus and critical energy release rate ("toughness") of the spacer layer. The particular geometry considered is shown in inset.

thickness cracking). For a tough polymer layer ( $\Gamma_p/\Gamma_c > 25$ ), the greatest  $\epsilon_c$  possible (labeled  $\epsilon_{\max}$ ) is realized for the MLD thickness of 8.5 nm. Here, simultaneous cracking is expected for  $h_p < 8.5$  nm, while fracture specific to the topmost ceramic layer is predicted for  $h_p > 8.5$  nm. The  $\epsilon_{\max}$  of 3.03% is roughly twice the  $\epsilon_c$  of 1.56% measured for 25 nm thick alumina films, Table I. As  $\Gamma_p/\Gamma_c$  is decreased to 10, through-thickness fracture corresponding to decreased  $\epsilon_c$  is predicted for  $h_p < 25$  nm, whereas fracture specific to the topmost layer corresponding to the maximum  $\epsilon_c$  of 2.94% is expected for  $h_p > 25$  nm. Performance is limited for a brittle polymer layer ( $\Gamma_p/\Gamma_c < 5$ ) and cracks are expected to always form through the entire thickness of the coating. Here, the maximum  $\epsilon_c$  is greatly reduced and does not strongly vary with  $h_p$ .

For the measured  $\Gamma$ , Tables I and II, the ratio  $\Gamma_p/\Gamma_c$  is determined to be  $\sim 0.05$ . For the composite coatings in Fig. 8, the analysis in Fig. 10 therefore affirms the measured  $\epsilon_c$  as well as the assertion that fracture occurs through their entire thickness. Figure 10 predicts the spacer layer will be ineffective at increasing  $\epsilon_c$ , analogous to the layer being absent. Specifically, if the alumina was made twice as thick, cracks would occur across the entire thickness and  $\epsilon_c$  would scale by a factor of  $1/\sqrt{2}$ , Eq. (4). As in the case of a single film on a substrate,<sup>34</sup> inelastic behavior in the substrate or spacer layers can greatly influence the strain/thickness relationship, which may also vary with loading rate, temperature, and specimen history.

In order to identify how the mechanical robustness of the three-layer composite system might be improved, the modeling was extended to examine a broad range of properties for the polymer layer, Fig. 11. Certain material properties were fixed (including  $E_c = 195.3$  GPa,  $\nu_c = 0.132$ ,  $\Gamma_c = 18.6$  J/m<sup>2</sup>,  $h_c = 25$  nm,  $\nu_p = 0.33$ ,  $E_s = 8.4$  GPa,  $\nu_s = 0.33$ , and  $h_s = 75$   $\mu$ m), while polymer specific properties ( $E_p$ ,  $\Gamma_p$ , and  $h_p$ ) were varied. The results, however, have been normalized so that they may be applied to a variety of similar multilayer architectures. As in Fig. 10, the regimes of simultaneous versus top-specific, through-thickness versus top-

specific, and through-thickness fracture apply to the conditions of high, intermediate, and low  $\Gamma_p/\Gamma_c$  values, respectively. The sequence of preferred failure mode (simultaneous, then top-specific, then through-thickness fracture) is common to all  $\Gamma_p/\Gamma_c$  examined, however the entire sequence is not realized within the range of  $E_p/E_c$  for all the profiles in Fig. 11. Specifically, for  $\Gamma_p/\Gamma_c > 1$ , the  $\varepsilon_{\max}$  solution is realized along the upper bound at the top of Fig. 11, corresponding to the condition of simultaneous or top-specific fracture. For  $\Gamma_p/\Gamma_c = 50$ , for example, the transition from simultaneous to top-specific fracture occurs at  $E_p/E_c \sim 0.25$ . For  $\Gamma_p/\Gamma_c = 10$ , departure from the upper bound at  $E_p/E_c \sim 0.4$  corresponds to the transition from top-specific to through-thickness fracture, which is the expected failure mode as  $E_p/E_c$  is increased further, including the lower bound in Fig. 11. For the range of  $E_p/E_c$  studied, the maximum 2.64 times improvement in  $\varepsilon_c$  is indicated as “max  $\varepsilon_c$ ” in the figure. As in Fig. 10, the  $h_p$  value yielding the maximum  $\varepsilon_c$  may be determined if  $\Gamma_p/\Gamma_c$  and  $E_p$  are known.

Figure 11 identifies  $K_{IC}$  of the polymer as the most important factor governing mechanical robustness. As in Fig. 10,  $K_{IC}$  for the spacer layer reduces  $\Gamma_p/\Gamma_c$  of the system, particularly once through-thickness fracture becomes the sole failure mode. Conversely, a greater  $\varepsilon_c$  is predicted if  $K_{IC}$  could be improved by at least an order of magnitude. Note that Figs. 10 and 11 apply to the minimal condition required for the steady state propagation of a channel crack under quasistatic loading. In practice,  $\varepsilon_c$  as well as the localization of damage might also be improved according to  $\Gamma_p/\Gamma_c$  for dynamic- or impact-loading conditions.

After  $K_{IC}$ ,  $E_p$  is the second most significant factor of influence. For most  $\Gamma_p/\Gamma_c$  values,  $\varepsilon_c$  may be modestly improved with  $E_p$ , making increased  $E_p$  desirable. The analysis in Fig. 11, however, applies to the case of an externally applied strain. In other cases, e.g., thermal misfit, increasing  $E_p$  may increase  $\varepsilon_r$ , compromising the robustness of the coating.

Proposed applications for ALD, MLD, and/or composite coatings include flexible liquid crystal displays, OLEDs, and photovoltaic modules.<sup>15</sup> Additional applications include packaging for medical devices, sensor skins, electronic circuits, and micro- and nanosystems. Many of the proposed applications involve the use of coatings for the purpose of encapsulation to prevent chemical (water and oxygen) permeation. Barrier coatings may also enable *in vivo* biological compatibility or reduced photodegradation. In composite barrier coatings, the permeability of the spacer layer must be considered in addition to  $\varepsilon_c$ .

As suggested in Fig. 11, the replacement of alucone with a tougher material would be expected to improve the performance of the composite coatings in Table III. A brief survey<sup>54,62</sup> identifies alternate polymeric materials such as poly(methyl methacrylate), polyvinyl chloride, and polyamide (nylon), where  $\Gamma_p/\Gamma_c$  is improved by at least one to two orders of magnitude. The toughest polymeric materials, including polycarbonate, polyetheretherketone, polyimide, and the various polyesters, improve  $\Gamma_p/\Gamma_c$  by at least two to four orders of magnitude. PEN serves as an excellent example of a tough polymer, as the material will endure extensive inelastic deformation (Fig. 3) and would be expected to tear (Fig.

9) and/or craze prior to ultimate failure. In contrast, various epoxies, rubbers, or silicones may bear improved  $\Gamma$ , but their low modulus or yield strength would limit  $\varepsilon_c$  of a composite coating. Aside from conventional polymeric materials, the study of the MLD technique is ongoing. Here, a wealth of chemical sequences may be utilized to increase the length of chemical chains, reorient the direction of growth, incorporate aromatic or other chain geometries, create bonding, and/or promote cross linking in the in-plane direction. MLD also benefits from a variety of compatible chemical sequences that would promote strong adhesion to alumina.

So long as the spacer layer is tough, e.g.,  $\Gamma_p/\Gamma_c \geq 5$ , Fig. 11 indicates that a larger modulus is desirable. In macroscopic polymeric materials, the modulus may be tailored according to the content of filler or stiffening material.<sup>62</sup> In ALD, a similar effect may be achieved by alternating between separate chemical sequences, yielding a single ceramic layer that itself consists of different monolayers of material.<sup>63</sup> The spacer layer could likewise contain layers composed of different organic molecules. Additional control of material properties may be possible if the porous content or bond density can be tailored according to the deposition parameters utilized in the ALD or MLD techniques, i.e., temperature, time, or pressure.

Aside from the deposited film(s), the performance of coatings may be influenced by the choice of substrate material. Equation (4) indicates that, if  $\Gamma_c$  remains the same, then  $\varepsilon_c$  will be improved if  $D_1$  is decreased, i.e.,  $E_s$  is increased. Many of the aforementioned applications require a flexible and transparent substrate. If a polymer is utilized, only marginal  $\varepsilon_c$  improvement may be possible. In cases where a more rigid substrate may be substituted for PEN, the substrate itself should have sufficient toughness and must not yield or fracture at a strain less than that of the coating.

## V. CONCLUSIONS

The mechanical robustness of nanometer-thick ALD alumina, molecular layer deposited (MLD) alucone, and laminated composite coatings composed of both materials was characterized as a function of applied strain. Key results include the following.

The fracture toughness of the individual materials was determined at the onset of steady state channel crack propagation using a thin films fracture mechanics model. The fracture toughness of alumina was  $1.89 \pm 0.10$  MPa m<sup>0.5</sup>, being comparable to thin film alumina grown using physical vapor deposition. The toughness of alucone, a representative of a recently developed class of materials, was found to be  $0.17 \pm 0.02$  MPa m<sup>0.5</sup>. While both materials proved to be brittle, significant improvement in the critical strain for crack propagation can be made by reducing the film thickness, which can be precisely implemented using the ALD and MLD techniques. For example, the critical strain was improved from  $0.88\% \pm 0.08\%$  (critical bending radius of 4.30 mm) to  $5.08\% \pm 0.06\%$  (minimum radius of 0.64 mm) when the thickness of alumina was reduced from 125 to 5 nm.

All coatings, deposited on polyethylene naphthalate (PEN) substrates, demonstrated a similar evolution of dam-



age morphology according to the applied strain, including channel crack initiation, crack propagation at the critical strain (where chemical permeation is expected to increase by orders of magnitude), crack densification up to saturation, followed by transverse crack formation (although alucone monolayer films did not form transverse cracks). Interaction between cracks is not expected during densification, based on their large separation distance. From the saturated crack density, the interfacial shear was estimated to be  $39.5 \pm 8.3$  or  $66.6 \pm 6.1$  MPa, for alumina or alucone, respectively, indicating excellent adhesion to PEN.

The use of alucone as a spacer layer, situated between alumina films, was found to reduce the critical strain at fracture. A fracture mechanics based formalism identified regimes where failure would occur either simultaneously in the ceramic layers, in the topmost layer, or through the thickness of all layers. The experimentally observed through-thickness damage morphology along with tearing specific to the PEN substrate confirmed that the degraded performance of the composite coatings is attributed to the toughness of the alucone. Analysis further identified that the critical strain could be increased through the use of a spacer material bearing both a greater fracture toughness and greater mechanical modulus. Alternately, the critical strain could be improved by the choice of a stiffer substrate material, if allowed by the application.

## ACKNOWLEDGMENTS

The authors wish to acknowledge Paul Rice of the University of Colorado at Boulder and the National Institute for Standards and Technology (NIST) in Boulder for his help performing FIB cross sectioning. The authors are also grateful to Ken Yabuki of DuPont/Teijin Films and Joan Taylor of Tekra Corp. for supplying PEN as well as Dr. Yu-Zhong Zhang of Invitrogen/Molecular Probes, Inc. for supplying the chemical tag. This work was supported by WiSpry Inc. through the DARPA Center on Nanoscale Science and Technology for Integrated Micro/Nano-Electromechanical Transducers (iMINT) funded by DARPA N/MEMS S&T Fundamentals Program (Grant No. HR0011-06-1-0048). This material is based upon work supported by the National Science Foundation under Grant No. IIP-0741177. Additional support was provided by the Air Force Office of Scientific Research.

- <sup>1</sup>M. Leskelä and M. Ritala, *Thin Solid Films* **409**, 138 (2002).
- <sup>2</sup>M. Ritala and M. Leskelä, *Angew. Chem. Int. Ed.* **42**, 5538 (2003).
- <sup>3</sup>A. W. Ott, J. W. Klaus, J. M. Johnson, and S. M. George, *Thin Solid Films* **292**, 135 (1997).
- <sup>4</sup>J. W. Elam, M. D. Groner, and S. M. George, *Rev. Sci. Instrum.* **73**, 2981 (2002).
- <sup>5</sup>M. Hong and J. Kwo, *ECS Trans.* **1**, 41 (2005).
- <sup>6</sup>A. A. Dameron, D. Seghete, B. B. Burton, S. D. Davidson, A. S. Cavanagh, J. A. Bertrand, and S. M. George, *Chem. Mater.* **20**, 3315 (2008).
- <sup>7</sup>S. M. George, B. H. Yoon, and A. A. Dameron, *Acc. Chem. Res.* **42**, 498 (2009).
- <sup>8</sup>M. D. Groner, S. M. George, R. S. McLean, and P. F. Carcia, *Appl. Phys. Lett.* **88**, 051907 (2006).
- <sup>9</sup>A. A. Dameron, S. D. Davidson, B. B. Burton, and P. F. Carcia, *J. Phys. Chem. C* **112**, 4573 (2008).
- <sup>10</sup>C. F. Herrmann, F. H. Fabreguette, D. S. Finch, R. Geiss, and S. M. George, *Appl. Phys. Lett.* **87**, 123110 (2005).
- <sup>11</sup>H. Kim, H. B. R. Lee, and W.-J. Maeng, *Thin Solid Films* **517**, 2563 (2009).
- <sup>12</sup>J. W. Elam, D. Routkevitch, P. D. Mardilovich, and S. M. George, *Chem. Mater.* **15**, 3507 (2003).
- <sup>13</sup>C. F. Herrmann, F. W. DelRio, D. C. Miller, S. M. George, V. M. Bright, J. L. Ebel, R. E. Strawser, R. Cortez, and K. D. Leedy, *Sens. Actuators, A* **135**, 262 (2007).
- <sup>14</sup>N. Cordero, J. Yoon, and Z. Suo, *Appl. Phys. Lett.* **90**, 111910 (2007).
- <sup>15</sup>G. L. Graff, P. E. Burrows, R. E. Williford, and R. F. Praino, in *Barrier Layer Technology for Flexible Displays*, Flexible Flat Panel Displays, edited by G. P. Crawford (Wiley, Hoboken, 2005).
- <sup>16</sup>M. K. Tripp, C. Stampfer, D. C. Miller, T. Helbling, C. F. Herrmann, C. Hierold, K. Gall, S. M. George, and V. M. Bright, *Sens. Actuators, A* **130–131**, 419 (2006).
- <sup>17</sup>D. C. Miller, R. R. Foster, S. H. Jen, J. A. Bertrand, S. J. Cunningham, A. S. Morris, Y. C. Lee, S. M. George, and M. L. Dunn, (unpublished).
- <sup>18</sup>D. C. Miller, R. R. Foster, S. H. Jen, J. A. Bertrand, D. Seghete, B. H. Yoon, Y. C. Lee, S. M. George, and M. L. Dunn, (unpublished).
- <sup>19</sup>J. L. Beuth, Jr., *Int. J. Solids Struct.* **29**, 1657 (1992).
- <sup>20</sup>J. W. Hutchinson and Z. Suo, in *Mixed Mode Cracking in Layered Materials. Advances in Applied Mechanics*, edited by J. W. Hutchinson and T. Y. Wu (Academic, San Diego, 1992), pp. 63–191.
- <sup>21</sup>M. D. Thouless, E. Olsson, and A. Gupta, *Acta Metall. Mater.* **40**, 1287 (1992).
- <sup>22</sup>L. B. Freund and S. Suresh, *Thin Film Materials: Stress, Defect Formation and Surface Evolution* (Cambridge University Press, Cambridge, 2003).
- <sup>23</sup>H. Mei, R. Huang, J. Y. Chung, C. M. Stafford, and H. H. Yu, *Appl. Phys. Lett.* **90**, 151902 (2007).
- <sup>24</sup>X. Wu and G. C. Weatherly, *Acta Mater.* **47**, 3383 (1999).
- <sup>25</sup>U. A. Handge, Y. Letterier, G. Rochat, I. M. Sokolov, and A. Blummen, *Phys. Rev. E* **62**, 7807 (2000).
- <sup>26</sup>Y. Leterrier, *Prog. Mater. Sci.* **48**, 1 (2003).
- <sup>27</sup>F. Delannay and P. Warren, *Acta Metall. Mater.* **39**, 1061 (1991).
- <sup>28</sup>R. Nahta and B. Moran, *Eng. Fract. Mech.* **52**, 513 (1995).
- <sup>29</sup>Z. C. Xia and J. W. Hutchinson, *J. Mech. Phys. Solids* **48**, 1107 (2000).
- <sup>30</sup>M. R. Begley and H. Bart-Smith, *Int. J. Solids Struct.* **42**, 5259 (2005).
- <sup>31</sup>D. C. Agrawal and R. Raj, *Acta Metall.* **37**, 1265 (1989).
- <sup>32</sup>M. S. Hu and A. G. Evans, *Acta Metall.* **37**, 917 (1989).
- <sup>33</sup>D. R. Wheeler and H. Osaki, in *Intrinsic Bond Strength of Metal Films on Polymer Substrates*, Metallization of Polymers, edited by S. P. Kowalkczyk (American Chemical Society, Washington, D.C., 1990).
- <sup>34</sup>J. L. Beuth and N. W. Klingbeil, *J. Mech. Phys. Solids* **44**, 1411 (1996).
- <sup>35</sup>A. L. Volynskii, S. Bazenov, O. V. Lebedeva, and N. F. Bakeev, *J. Mater. Sci.* **35**, 547 (2000).
- <sup>36</sup>M. D. Thouless, *J. Am. Ceram. Soc.* **76**, 2936 (1993).
- <sup>37</sup>Z. Y. Huang, W. Hong, and Z. Suo, *J. Mech. Phys. Solids* **53**, 2101 (2005).
- <sup>38</sup>H. Jiang, D. Y. Khang, J. Song, Y. Sun, Y. Huang, and J. A. Rogers, *Proc. Natl. Acad. Sci. U.S.A.* **104**, 15607 (2007).
- <sup>39</sup>J. M. Ambrico and M. R. Begley, *Thin Solid Films* **419**, 144 (2002).
- <sup>40</sup>H. H. Yu and J. W. Hutchinson, *Int. J. Fract.* **113**, 39 (2002).
- <sup>41</sup>T. Nakamura and S. Kamath, *Mech. Mater.* **13**, 67 (1992).
- <sup>42</sup>W. A. MacDonald, *J. Mater. Chem.* **14**, 4 (2004).
- <sup>43</sup>W. A. MacDonald, K. Rollins, D. MacKerron, K. Rakos, R. Eveson, K. Hashimoto, and B. Rustin, in *Engineered Films for Display Technologies*, Flexible Flat Panel Displays, edited by G. P. Crawford (Wiley, Hoboken, 2005).
- <sup>44</sup>ASTM International, "Standard test method for tensile properties of thin plastic sheeting," ASTM Report No. D882–02, 2002.
- <sup>45</sup>ASTM International, "Standard test method for tensile properties of plastics," ASTM Report No. D638–03, 2003.
- <sup>46</sup>Y. Zhang *et al.* (unpublished).
- <sup>47</sup>B. A. Banks, S. K. Rutledge, and K. K. deGroot, NASA Tech. Memo, NAS 1.15:106855 (1995) (National Aeronautics and Space Administration).
- <sup>48</sup>A. S. da Silva Sobrinho, G. Czeremuszkin, M. Latrèche, and M. R. Werthiemer, *J. Vac. Sci. Technol. A* **18**, 149 (2000).
- <sup>49</sup>S. Grego, J. Lewis, E. Vick, and D. Temple, *Thin Solid Films* **515**, 4745 (2007).
- <sup>50</sup>J. A. Knapp, D. M. Follstaedt, S. M. Meyers, J. C. Barbour, and T. A. Friedmann, *J. Appl. Phys.* **85**, 1460 (1999).
- <sup>51</sup>S. Grego, J. Lewis, E. Vick, and D. Temple, *J. Soc. Inf. Disp.* **13**, 575 (2005).
- <sup>52</sup>D. R. Cairns and G. P. Crawford, *Proc. IEEE* **93**, 1451 (2005).
- <sup>53</sup>S. Wagner, H. Gleskova, I.-C. Cheng, J. C. Sturm, and Z. Suo, in *Mechan-*

- ics of TFT Technology on Flexible Substrates*, Flexible Flat Panel Displays, edited by G. P. Crawford (Wiley, Hoboken, 2005).
- <sup>54</sup>W. D. Callister, *Materials Science and Engineering: An Introduction*, 4th ed. (Wiley, Hoboken, 1996).
- <sup>55</sup>J. Thurn and R. F. Cook, *J. Mater. Res.* **39**, 4809 (2004).
- <sup>56</sup>V. A. C. Haanappel, H. D. von Corbach, T. Fransen, and P. J. Gellings, *Mater. Sci. Eng., A* **167**, 179 (1993).
- <sup>57</sup>M. Yanaka, B. M. Henry, A. P. Roberts, C. R. M. Grovenor, G. A. D. Briggs, A. P. Sutton, T. Miyamoto, Y. Tsukahara, N. Takeda, and R. J. Chater, *Thin Solid Films* **397**, 176 (2001).
- <sup>58</sup>A. P. Jackson, J. F. V. Vincent, and R. M. Turner, *Proc. R. Soc. London, Ser. B* **234**, 415 (1988).
- <sup>59</sup>T. W. Clyne and P. J. Withers, *An Introduction to Metal Matrix Composites* (Cambridge University Press, Cambridge, 1993).
- <sup>60</sup>L. Chandra and T. W. Clyne, *Diamond Relat. Mater.* **3**, 791 (1994).
- <sup>61</sup>S. Hashemi and A. Arkhireyeva, *J. Macromol. Sci., Phys.* **B41**, 863 (2002).
- <sup>62</sup>M. A. Meyers and K. K. Chawla, *Mechanical Behavior of Materials* (Prentice-Hall, Upper Saddle River, 1999).
- <sup>63</sup>J. W. Elam, Z. A. Sechrist, and S. M. George, *Thin Solid Films* **414**, 43 (2002).